A NUMERICAL TECHNIQUE FOR MODELLING HYPERSONIC INFLATABLE SHIELDS

V. Orlandini*, R. Paciorri*, A. Assonitis*, F. Saltari*, F.Mastroddi* and A. Bonfiglioli†

* University of Rome "La Sapienza"
Via Eudossiana 18, 00184 Rome, Italy

† Università degli Studi della Basilicata
Viale dell'Ateneo Lucano 10, 85100 Potenza, Italy

Key words: Front tracking, Shock-Fitting, Inflatable Structures

Summary. This paper describes a recently developed numerical technique to simulate high-speed flows on complex 3D inflatable structures using tetrahedral volume grids. In detail, the proposed methodology is based on the front-tracking approach, as it involves the coupling between a shock-fitting technique and a non-linear structural solver: by doing so, we are able to exploit the well-known advantages of shock-fitting regarding the computation and modelling of gas-dynamic discontinuities to deal with fluid-structure interaction problems. More details about the proposed technique and some applications to inflatable structures in hypersonic flows are presented in this paper.

1 INTRODUCTION

Fluid-structure interaction (FSI) problems involve interactions of movable and/or deformable structures with a surrounding fluid flow. These phenomena are commonly encountered in both engineering and biological applications, which range for instance from wind turbines to blood flow in arteries. Concerning aerospace applications, FSIs are particularly relevant when dealing with tank-fuel sloshing [1], aircraft wings[2] as well as supersonic parachutes [3]. For this reason, many studies were carried out on this subject, proposing different methodologies.
In this work, we present a novel fluid dynamic technique for computing high speed flows past hypersonic inflatable shields (HIADs): specifically, it is based on a shock-fitting (S-F) method [4], which models gas dynamic discontinuities, such as shock waves, as surfaces of null thickness bounding regions of the flow-field where a smooth solutions to the governing PDEs exists. Moreover, the space-time evolution of these discontinuities, as well as their upstream/downstream states, are provided by enforcing the Rankine-Hugoniot (R-H) jump relations. S-F allows to overcome most of the troubles encountered by the widely used shock-capturing (S-C) schemes when dealing with shocked-flows. These drawbacks

1

include: a "captured" shock-width which exceeds by orders of magnitude the physical one and the presence of spurious disturbances along the "captured" shock-front which spoil the solution in the entire shock-downstream region, see Refs. [5, 6, 7, 8].

Even though S-F methods were designed for modelling gas-dynamic discontinuities, a similar approach can be used to represent inflatable structures, which are generally modeled as membranes [9], i.e. as thin structures of negligible thickness. Following this idea, thin membranes can be considered as discontinuities within the flow field, just like shock waves and, therefore, are modelled using zero-thickness surfaces. However, while the displacement of the gas-dynamic discontinuities is computed by enforcing the jump relations, the displacement of the structure is provided by a structural solver according to the values of the loads determined by the inflation pressure and by the external fluid-dynamic field acting on the membrane wall. Even though the modelling approach described here is similar to those reported in previous studies, which simulate FSI in supersonic flows using front-tracking techniques [3, 10], there are also some differences. First of all, in the aforementioned publications front-tracking was limited to the modelling of the deformable structure, whereas the gas-dynamic discontinuities were modeled using shock-capturing. Moreover, compared to the commonly used immersed-boundary methods [11], our approach does not require any interpolation/extrapolation to prescribe boundary conditions on the wall. Indeed, as will be clarified in Section 2, we perform a local re-meshing of the volume mesh around the surfaces of both the shock and the inflatable shield. By doing so, these surfaces are constrained to be part of the computational grid, so that boundary conditions on the inflatable wall can be straightforwardly applied.

Algorithmic details about the proposed methodology are given in Section 2. Furthermore, the application of this novel technique to two FSI test-cases involving inflatable shields in hypersonic flows is presented, including a quantitative investigation of the error reduction obtained with the proposed approach, using both a global and local grid-convergence analysis.

2 METHODOLOGY

Numerical simulations reported in this study are computed using a numerical technique for FSI based on the S-F approach. More precisely, the aforementioned methodology is the most recent enhancement in the development of a three-dimensional S-F code for unstructured grids *UnDiFi-3D*, developed by some of the authors and described in Ref. [7]. In this approach, the behaviour of the membranes is modelled and computed by coupling the *UnDiFi-3D* solver with the non linear structural solver MSC Nastran [12], in order to exploit for the first time the advantages offered by S-F in the context of FSI simulations. To briefly describe this novel technique, Figure 1 shows the hypersonic flow past an inflatable shield, leading to the formation of a bow-shock in the proximity of the inflatable wall. Both the bow-shock and the inflatable wall are represented by surfaces of zero thickness, resp. coloured in blue and red in Fig.1. The FSI simulation starts from a solution supplied by a S-C solver, treating the shield as a rigid body. This solution is

used as the initial condition for the S-F computation: details concerning the shock-surface extraction from this initial S-C solution and the shock modelling in the *UnDiFi-3D* solver are available in Refs. [7, 8]. The tetrahedral grid used in the S-C calculation shall be referred to in the following as the "background" mesh.

The FSI algorithm can be split into the following five main steps:

1. *Step 1 : Generation of the computational mesh*
   The shock surface is inserted into the background tetrahedral mesh, which was used for computing the S-C solution. In doing so, all cells of the background mesh that are crossed by shock surface are removed. This step is performed only once, in order to initialize the FSI algorithm. This newly created "computational" grid, thus containing the shock points, is given as input to the FSI algorithm, as shown in Fig.1.

2. *Step 2: CFD solver*
   Once the computational grid has been generated as described in Step 1, solution values within all grid and shock points are advanced over a single (pseudo) time-step using the in-house, unstructured, S-C, CFD code `eulfs` [13], which has second order spatial accuracy.

3. *Step 3: MSC Nastran nonlinear finite element solver on the two faces of the inflatable shield.*
   At this point, the structural deformation of the HIAD is computed using the membrane non-linear solver, SOL 400 of MSC Nastran [12], that takes into account both the inflation pressure and the aerodynamic loads computed by the `eulfs` solver.
   It is worth underlying, see Fig.2, that we chose to mesh the inflatable shield using quadrangular elements, instead of the triangular ones used for discretizing the shock surface, because quadrilateral elements make iterative convergence of the structural solver more robust. For this reason, each quadrangular element of the structural mesh in Fig. 2 is split into two triangles when it is fed to the CFD solver. By doing so, the triangulated surface describing the inflatable wall for the CFD solver shares the same nodes with the quadrangular grid used for the structural analysis, so that no interpolation is required to transfer the dependent variables from the CFD solver to the structural one. Moreover, grid-points located along the nose of the HIAD, marked using a red line in Fig. 2, are constrained to move only in the flow direction because they are anchored to a rigid nose that can only move along the capsule's symmetry axis. On the contrary, the peripheral nodes of the inflatable structure, marked using a blue line in Fig. 2, can only move in the plane normal to the flow direction. Finally, Fig. 3 shows the loads acting on the inflatable wall: the red arrows represent loads due to the constant inflation pressure, whereas the black arrows represent those of the external pressure calculated by `eulfs`; their differential magnitude governs the displacement of the thin shield. This structural model aptly

3

mimics the inflation and deflation behavior of the shield, and it will play a crucial role for applying the FSI algorithm to drag modulation.

4. *Step 4: Solution update within the shock-nodes*
   As explained in detail in Ref. [7], the shock-downstream values of the dependent variables within the shock-points need to be corrected by enforcing the R-H jump relations within each shock-point. The R-H equations also provide the local shock-speed, which allows to compute the new shock position.

5. *Step 5: Shock and wall points displacement*
   Because of the displacement of both the inflatable wall and the shock-points, the computational grid needs to be remeshed. This is accomplished using the Tet-Gen [14] mesh generator, which provides a new computational mesh to be used as input to restart the FSI algorithm from step 2, until steady-state is reached.
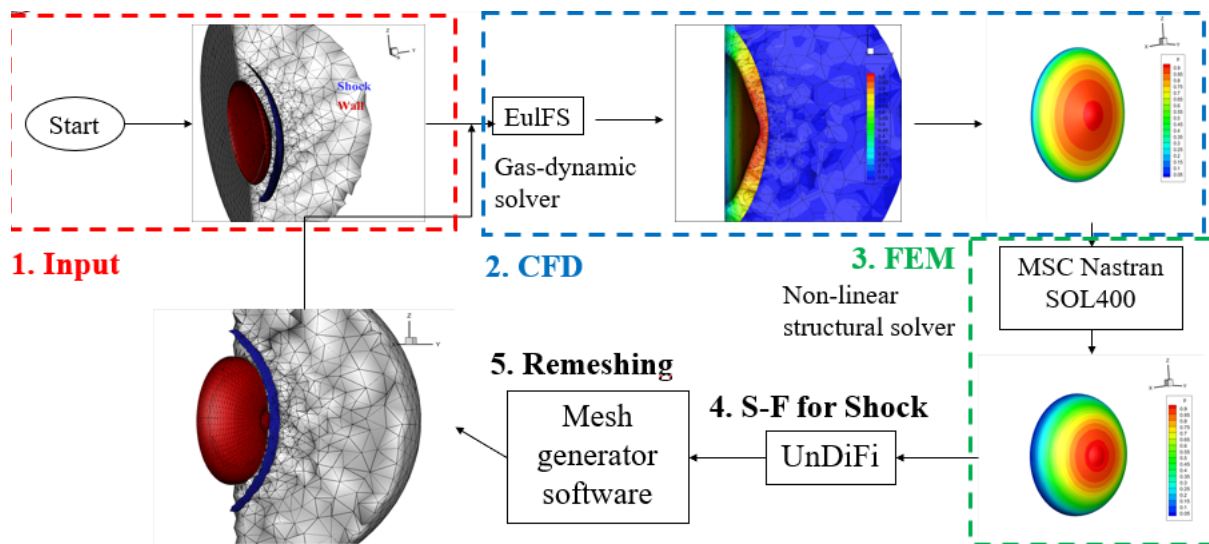

Figure 1: FSI algorithm flowchart

3   NUMERICAL SIMULATION OF FSI INTERACTION OF AN INFLAT-ABLE SHIELD

In this section we will analyze and discuss the results obtained from the simulation of an inviscid high-speed flow past a HIAD. More precisely, the Mach 24 hypersonic flow past an inflatable shield is used as a benchmark for the proposed technique; more specifically, this test-case simulates the flow conditions during an aerocapture mission on Mars, which we proposed as a viable application for inflatable shields in Ref. [15]. In order to evaluate also the grid-convergence properties, calculations have been performed using two nested
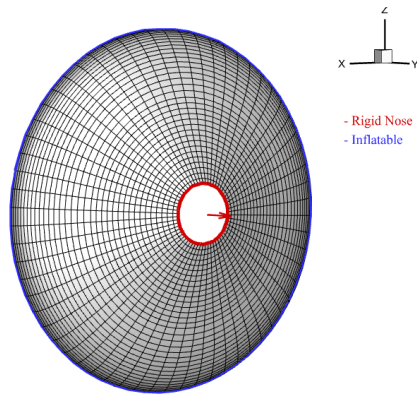
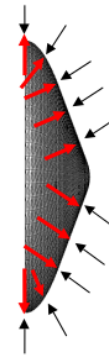**Figure 2**: Inflatable shield surface: structured grid for FEM solver

Figure 3: Internal and external loads

grid levels, the finest one obtained by splitting each cell of the coarsest mesh into eight tetrahedra. Figure 4 shows half of the computational domain and the coarsest volumetric grid: it consists of an hemisphere representing the fluid-dynamic field, with the shock surface highlighted in blue and the inflatable shield in green.
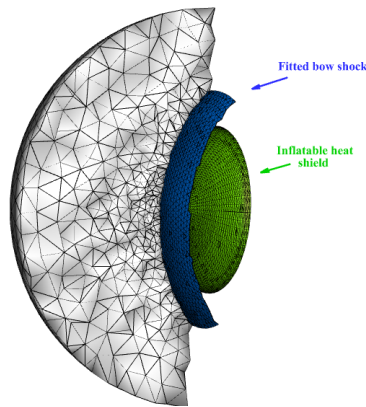

Figure 4: Half computational domain and coarsest grid

The atmospheric conditions during the aerocapture maneuver reported in Ref. [15] correspond to an altitude of 50 km above the Martian surface. At this altitude, the Mars Climate database [16, 17] gives a density value equal to $\rho = 9.74 \cdot 10^{-5} kg/m^3$ and a free-stream pressure p_∞ equal to 3.23 Pa. Furthermore, it is noted that the Martian atmosphere primarily consists of CO_2, accounting for 95% of the composition. CO_2 is characterized by an adiabatic constant γ of 1.33 and a specific gas constant R of 191 J/kgK. These atmospheric parameters are crucial for accurate analysis and modeling of hypersonic flow around inflatable shields on Mars. Indeed, we can use the jump relations

for the analytical calculation of the stagnation point pressure p_{st}:

$$p = p_\infty(1 + \frac{2\gamma}{\gamma + 1}(M_\infty^2 - 1))$$

$$M_{sv} = \sqrt{\frac{1 + \frac{\gamma-1}{2}M_\infty^2}{\gamma M_\infty^2 - \frac{\gamma-1}{2}}} \tag{1}$$

$$p_{st} = p_\infty(1 + \frac{\gamma - 1}{2}M_{sv}^2)^{\frac{\gamma}{\gamma-1}}$$

where p_∞ is the static pressure, M_∞ the upstream Mach number, M_{sv} the shock-downstream Mach number and p_{st} is the stagnation pressure that in these conditions is determined to be 2307.45 Pa.

Some considerations regarding the inflatable shield modelling can be drawn. First of all, Kevlar has been chosen as the material for the inflatable portion with a thickness of 1 mm, moreover the shield is inflated to a pressure $p_{inf} = 3462$ Pa, corresponding to 1.5 times the stagnation point pressure. It is important to mention that, in these preliminary results, the rotational degrees of freedom of the structural model have been constrained in order to enhance the convergence of the structural simulations and to overcome the buckling problems that occur. Figure 5 illustrates the pressure flow field on symmetry plane YZ
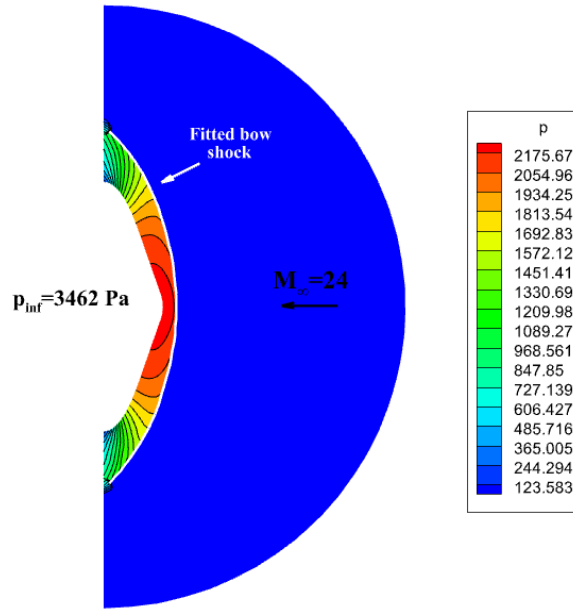

Figure 5: Hypersonic flow past an inflatable shield: pressure flow field on symmetry plane YZ

provided by the FSI algorithm previously described. The advantages provided by the S-F are self-evident: the bow shock exhibits null thickness and a smooth pressure distribution

is provided in the shock layer. Figure 6, which compares the wall pressure distribution on the two grid levels, highlights a further advantage related to the S-F approach: the S-F calculation reveals a good circumferential symmetry already on the coarse grid, despite the use of a fully unstructured tetrahedralization. Thus, S-F is able to provide high quality solution also using coarse meshes, meaning in computational costs savings.
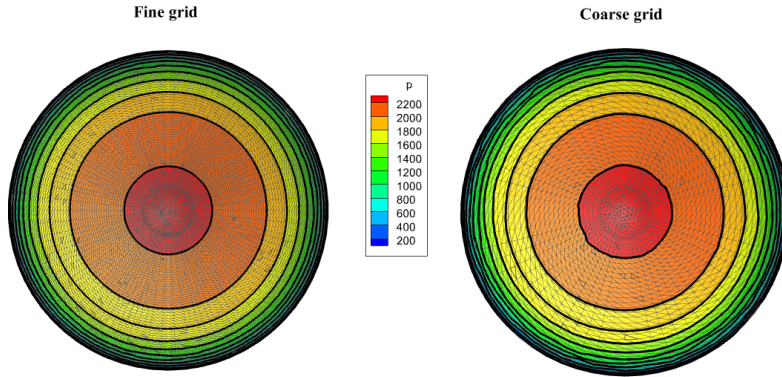

Figure 6: Wall pressure distribution on both the coarse and fine grids

A grid-convergence analysis of the FSI technique is hereafter presented by measuring the global total temperature, T_0, error, taking into account that T_0 is constant in the whole computational domain. In particular, the observed order of accuracy, $\tilde{n}$, has been calculated using the following equations, as stated in Ref. [18, 19]:

$$\tilde{n} = \frac{\log R^{-1}}{\log r} \qquad (2)$$

where the grid refinement ratio is equal to $r = 2$ for nested meshes and the grid convergence ratio R is given by Eq. (3):

$$R = \frac{u_2 - u_0}{u_1 - u_0} \qquad (3)$$

where u_i denotes the flow variable used for evaluating the order of accuracy computed on i^{th} grid level, the subscripts 1 and 2 resp. refer to the coarse and fine grid-levels, whereas the subscripts 0 denotes the exact solution, which in our case is the constant, free-stream dimensionless total temperature. Table 1 shows the values of the L_1 norm of the discretization error based on T_0 for both grid levels and the observed order of accuracy computed using Eq. (2). The observed order of accuracy is seen to be close to design order, $n = 2$, which implies that both the coarse- and the fine-grid solutions are in asymptotic convergence. This is further confirmed by the fact that the discretization error is reduced by a factor R^{-1} nearly equal to four, when moving from the coarse to the fine mesh. Moreover, it is worth noting that the error on the coarsest mesh is less that 1% of the total temperature value.

Table 1: L_1 norm of the discretization error on the coarse and on the fine mesh.

$u_1 - u_0$	$u_2 - u_0$	$\tilde{n}$
5.718e-04	1.608e-04	1.83

A local grid-convergence analysis has also been performed by measuring the discretization error at the stagnation point. Table 2 allows to compare the stagnation pressure computed by the UnDiFi gas-dynamic solver with the analytical value computed using Eq. (1); the dimensionless discretization error ϵ is also shown. The observed order of accuracy is seen to be close to design order, as it happens to be the case with the global analysis based on total temperature.

Table 2: Local convergence analysis: comparison between computed and analytical stagnation pressure.

Grid level	Analytical p_{st} (Pa)	Numerical p_{st} (Pa)	ϵ
1	2307.45	2304.53	0.0012669
2	2307.45	2306.6	0.0003698
order of convergence $\tilde{n}$			1.7765

4 COMPLETE INFLATABLE STRUCTURE CONFIGURATION

This section describes a new test-case, similar to the previous one used for the convergence analysis, where is also modelled the rear part of the inflatable structure. The presented geometry is inspired by the ESA Efesto capsule engineered for re-entry into Mars atmosphere. The initial geometry is considered fully inflated at an inflation pressure of 20 kPa (this is a typical value for the inflation pressure). Since the Finite Element Model (FEM) is built by assuming this configuration, the structure must exhibits a certain stress state determined by this configuration. Thus, we derive the stress following this procedure:

1. start from the inflated configuration;

2. compute the solution by imposing the maximum inflation pressure without FSI;

3. extract the stress state.

This stress state is then integrated into the FEM model using the "$ISTRESS$" function available in MSC Nastran. Consequently, when the inflation pressure is set to 20 kPa, the shield does not deform, while applying a lower inflation pressure the shield deflates.

Figure 8 depicts the structural model, which employs a quadrilateral mesh on the inflatable part, in contrast to the CFD solver that requires triangular elements, as in the
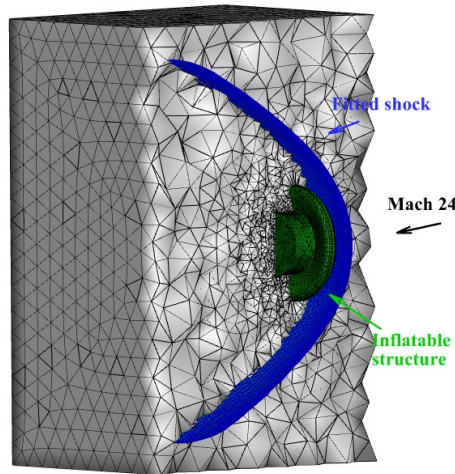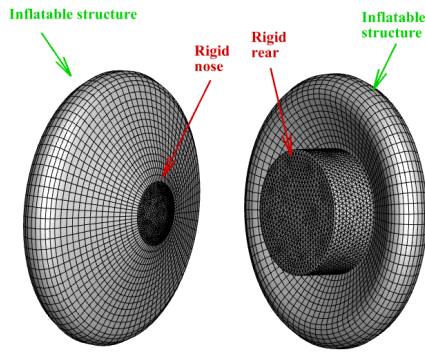
Figure 7: Computational domain

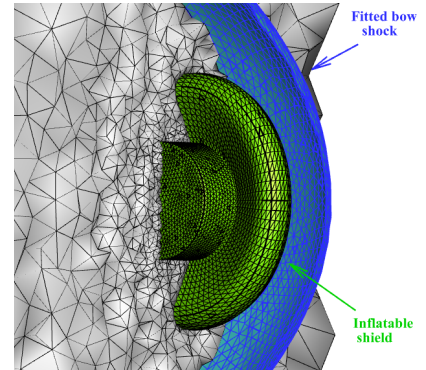**Figure 8**: Inflatable shield surface: structured grid for FEM solver

Figure 9: Rear view of the computational domain in Fig.7

previous case. Consequently, as explained in Sec. 2, the squares of the structural mesh are split into triangles to preserve the same nodes, thus avoiding interpolation to transfer data from the CFD to the structural solver.

For this test case, the computational domain shown in Fig.7 and 9 is considered. Also in this case, numerical computation involves Martian atmosphere with the same freestream conditions described in the previous test-case, along with two different inflation pressures: 2600 Pa and 20 kPa. The former was chosen to represent a deflated scenario, while the latter represents the fully inflated structure. Figures 10 and 11 show the solutions in terms of pressure field on the symmetry plane YZ: as in the previous test-case, similar considerations regarding solution quality improvement due to S-F can be made evaluating these images.

Figure 12 illustrates the effect of the MSC Nastran ISTRESS function: at pressures below 20 kPa, the structure tends to deflate, as observed in the cases represented by the black
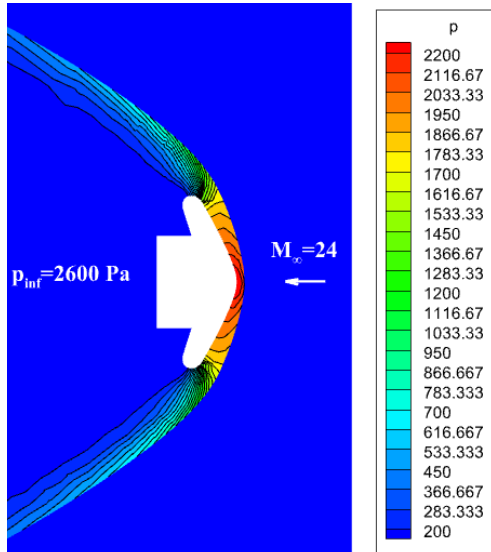
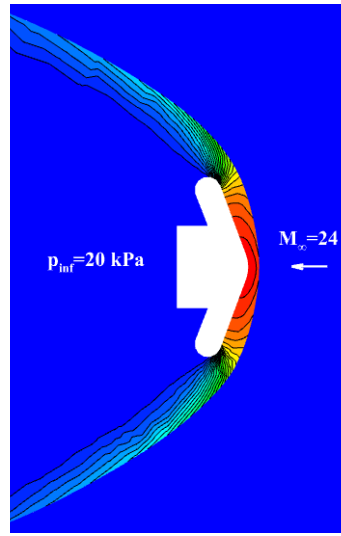**Figure 10**: Pressure field on plane YZ ($p_{inf} = 2600Pa$)

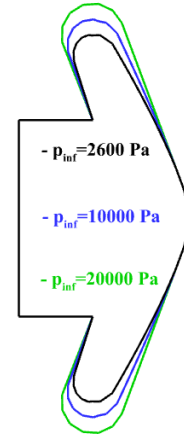**Figure 11**: Pressure field on plane YZ ($p_{inf} = 20kPa$)

Figure 12: Side view of the structure at different inflation pressures

(2600 Pa) and blue (10 kPa) lines, while remaining unchanged at 20 kPa. It is noteworthy that the external fluid dynamic field does not exert a significant influence in this scenario, as the pressure field exhibits values lower than 2300 Pa. To observe its effect, lower inflation pressures should be considered.

Inflatable shields lend themselves well to drag modulation techniques, which amounts to alter the drag during a reentry or aerocapture maneuver to achieve trajectories with less critical thermal loads or to compensate the unforeseen variations in atmospheric density on the target planet. For example, Table 3 shows the different values of aerodynamic drag, computed using $D = \frac{1}{2}\rho_\infty C_D A U_\infty^2$, for each configuration in Fig. 12 and the percentage variation w.r.t. the fully inflate shield. Since by continuously modulating the inflation pressure of the shield we modify the product $C_D A$, we are able to continuously change the spacecraft drag in order to follow a target trajectory, as proposed in Ref. [15].

Table 3: Aerodynamic drag of three different inflation pressures

p_{inf} (kPa)	D (N)	ϵ
20	124142.47	
10	104933.69	15.47%
0.26	88031.52	29.08%

5 CONCLUSION AND FUTURE WORK

In this study a novel numerical technique for computing fluid-structure interaction on

inflatable structures in high speed flows has been presented. This methodology derives from shock-fitting methods that explicitly identify and track the motion of gas-dynamic discontinuities within the flow-field, modelling them as internal boundaries in the computational domain. Following this approach, a similar model for describing inflatable structures was considered for thin structures of negligible thickness. Therefore, we developed a solver for computing fluid-structure interaction problems that couples a non linear structural solver with a shock-fitting gas-dynamic code, developed in the past years by some of the authors. By doing so, we were capable of exploiting the advantages in terms of flow-field solution quality provided by shock fitting, as highlighted by the two test-cases included in this paper. An analysis of both local and global grid-convergence of this novel technique showed that observed order-of-convergence was very close to the theoretical one: moreover, it showed small errors even on the coarsest grid level. Further developments of the proposed technique, such as viscosity effects in the flow-field as well as non-isotropic material behaviour for the wall, will be subject of future work.

ACKNOWLEDGMENTS

REFERENCES

[1] F. Saltari, A. Traini, F. Gambioli, and F. Mastroddi, "A linearized reduced-order model approach for sloshing to be used for aerospace design," *Aerospace Science and Technology*, vol. 108, p. 106369, 2021.

[2] R. Kamakoti and W. Shyy, "Fluid–structure interaction for aeroelastic applications," *Progress in Aerospace Sciences*, vol. 40, no. 8, pp. 535–558, 2004.

[3] J.-D. Kim, Y. Li, and X. Li, "Simulation of parachute FSI using the front tracking method," *Journal of Fluids and Structures*, vol. 37, pp. 100–119, 2013.

[4] R. Paciorri and A. Bonfiglioli, "A shock-fitting technique for 2d unstructured grids," *Computers & Fluids*, vol. 38, no. 3, pp. 715–726, 2009.

[5] R. Paciorri and A. Bonfiglioli, "Shock interaction computations on unstructured, two-dimensional grids using a shock-fitting technique," *Journal of Computational Physics*, vol. 230, no. 8, pp. 3155–3177, 2011.

[6] L. Campoli, A. Assonitis, M. Ciallella, R. Paciorri, A. Bonfiglioli, and M. Ricchiuto, "UnDiFi-2D: an unstructured discontinuity fitting code for 2d grids," *Computer Physics Communications*, vol. 271, p. 108202, 2022.

[7] A. Bonfiglioli, M. Grottadaurea, R. Paciorri, and F. Sabetta, "An unstructured, three-dimensional, shock-fitting solver for hypersonic flows," *Computers & Fluids*, vol. 73, pp. 162–174, 2013.

[8] A. Assonitis, R. Paciorri, C. F. Ollivier Gooch, and A. Bonfiglioli, "3D flow computations over blunt bodies at hypersonic speeds using shock-fitting technique," in *AIAA AVIATION 2022 Forum*, p. 3989, 2022.

[9] J. Wu, Z. Zhang, A. Hou, M. Zhu, and Q. Wang, "Nonlinear structural dynamics of the inflatable re-entry vehicle experiment (IRVE)," in *22nd AIAA International Space Planes and Hypersonics Systems and Technologies Conference*, p. 5204, 2018.

[10] J. Boustani, M. F. Barad, C. C. Kiris, and C. Brehm, "Fully-coupled fluid-structure interaction simulations of a supersonic parachute," in *AIAA Aviation 2019 Forum*, p. 3279, 2019.

[11] F. Sotiropoulos and X. Yang, "Immersed boundary methods for simulating fluid–structure interaction," *Progress in Aerospace Sciences*, vol. 65, pp. 1–21, 2014.

[12] MSC.Nastran, "Release guide," *MSC Software Corporation*, 2004.

[13] A. Bonfiglioli, "Fluctuation splitting schemes for the compressible and incompressible euler and navier-stokes equations," *International Journal of Computational Fluid Dynamics*, vol. 14, no. 1, pp. 21–39, 2000.

[14] H. Si, "Tetgen, a delaunay-based quality tetrahedral mesh generator," *ACM Trans. Math. Softw.*, vol. 41, feb 2015.

[15] V. Orlandini, R. Paciorri, A. Assonitis, F. Saltari, and A. Bonfiglioli, "A fluid dynamics technique for modelling inflatable shield for re-entry or aerocapture missions," in *AIAA AVIATION 2023 Forum*, p. 4425, 2023.

[16] E. Millour, F. Forget, and S. Lewis, "Mars climate database v. 5.1. user manual," *ESTEC Contract*, vol. 11369, p. 95, 2014.

[17] F. Forget, "Improved general circulation models of the martian atmosphere from the surface to above 80 km," *Journal of Geophysical Research*, pp. 24155–24175.

[18] A. Bonfiglioli and R. Paciorri, "Convergence analysis of shock-capturing and shock-fitting solutions on unstructured grids," *AIAA journal*, vol. 52, no. 7, pp. 1404–1416, 2014.

[19] A. Di Mascio, R. Paciorri, and B. Favini, "Truncation error analysis in turbulent boundary layers," *J. Fluids Eng.*, vol. 124, no. 3, pp. 657–663, 2002.